RSC Advances

PAPER

View Article Online
View Journal | View Issue

Cite this: *RSC Adv.*, 2017, **7**, 13340

Fabrication of Co_3O_4 nanoparticles in thin porous carbon shells from metal–organic frameworks for enhanced electrochemical performance†

Bin Qiu, Wenhan Guo, Zibin Liang, Wei Xia, Song Gao, Qingfei Wang, Xiaofeng Yu, Ruo Zhao and Ruqiang Zou*

Received 16th December 2016
Accepted 9th February 2017

DOI: 10.1039/c6ra28296b

rsc.li/rsc-advances

Cobalt oxides, typically Co_3O_4, have received considerable attention due to their high theoretical capacity as anode materials for Li-ion batteries. However, their poor electron conductivity and large volume change upon the insertion/removal of Li^+ ions limit their practical application. Carbon coating is widely used to improve the electrochemical performance of materials and release the strain during the lithiation/delithiation processes, in which the thickness of the coating carbon shell has a vital role in determining the performance of the material. In this study, Co_3O_4 nanoparticles coated with a thin carbon shell are obtained from the metal–organic framework (MOF) precursor Co-MOF-74 *via* a sequential two-step carbonization process, where carbon oxides, *e.g.*, CO_2, are used as the oxidation atmosphere in the second step. The carbon content and shell thickness are controlled by changing the calcination time. The electrode containing a certain carbon content (3.17 wt%) exhibits a capacity of 1137 mA h g^{-1} after 100 cycles tested at 100 mA g^{-1} between 0.005 and 3.0 V. This enhanced electrochemical performance is attributed to the well-dispersed nanosized Co_3O_4 particles and thin carbon shell coating on the electrode surface, which shorten the Li^+ ion diffusion length and enhance the electron conductivity of the hybrid.

Introduction

Lithium ion batteries (LIBs) have attracted considerable attention with the development of mobile electronics and electric vehicles.[1] Numerous studies have focused on electrode materials, separators, and electrolytes.[2,3] Specifically, the anode material is regarded as one of the key elements in the construction of lithium ion batteries. Since Poizot *et al.* first reported the mechanism of transition oxides (CoO, FeO, NiO and CuO) as lithium storage materials,[4] metal oxides have attracted great attention due to their high theoretical capacities (much higher than that of graphite ~372 mA h g^{-1}) and low cost.[5,6] In particular, oxides of cobalt (CoO, Co_3O_4, *etc.*) have been widely investigated, and much progress has been made in Li-ion storage capacities.[7–10] However, there are still some disadvantages, such as fast capacity fading and large volume change during the lithiation and delithiation process, that severely limit their further application. To address these issues, two main types of strategies have been adopted. The first method focuses on the design of special structures (hollow spheres and polyhedral structures).[11,12] The special structures of electrode materials are believed to facilitate the diffusion of lithium ions and release the mechanical strain.[13] The second approach is carbon coating,[14] where carbon acts as a layer to buffer large volume changes, mitigate the aggregation of particles and increase the electronic conductivity of electrodes.[15]

Metal–organic frameworks (MOFs) are a family of microporous crystalline polymers with a high surface area and porosity, and are constructed from metal-containing clusters and organic ligands.[16] They have been widely used in gas storage/separation, chemical sensing, heterogeneous catalysis, bioimaging, drug delivery and luminescence.[17,18] Inheriting these properties, MOF-derived materials, including porous carbon, metals, metal oxides and metal sulphides, also show high surface areas, high pore volumes and tunable pore size distributions.[19] Furthermore, the obtained metals/metal oxides are well-dispersed in the carbon matrix, which contributes to a good electrochemical performance. Recently, transition metal oxides (Fe_2O_3, Co_3O_4, NiO and MnO) made from MOFs have been widely used as anodes for lithium-ion batteries.[20–25] In the preparation process for these methods, metal oxides/carbon hybrids are derived from MOFs mainly through two ways. The first way is through a sequential two-step heat treatment in which metal/carbon hybrids are first obtained under inert atmosphere, and then air is used as the oxidation gas to obtain metal oxides/carbon

Beijing Key Laboratory for Theory and Technology of Advanced Battery Materials, Department of Materials Science and Engineering, College of Engineering, Peking University, Beijing 100871, P. R. China. E-mail: rzou@pku.edu.cn

† Electronic supplementary information (ESI) available. See DOI: 10.1039/c6ra28296b

hybrids.[26,27] The second is the direct carbonization of MOFs under air atmosphere.[28–30] In both methods, control over the content and thickness of the carbon coating is essential for the battery performance of the final metal oxides/carbon hybrid electrodes. A thin porous carbon shell layer may enhance the electrochemical properties, but a thick amorphous carbon coating on the electrode may hinder the transportation of Li^+ through the interface between the electrolyte and electrode solid phase, leading to the depletion of battery performance.[31a] Metal oxides can be obtained through carbonization under a CO_2 atmosphere. Using CO_2 as the oxidation atmosphere, carbon can be kept and at the same time the metal can be oxidized to metal oxide with a carbon coating on its surface.[31b,c] This method is very convenient and could open a new way for the synthesis of metal oxides/carbon composites derived from metal organic frameworks. To date, no reports have focused on controlling the surface carbon coating of electrodes. Herein, we develop a simple method to prepare metal oxides/carbon hybrids derived from a cobalt MOF *via* two heat-treatment steps, using carbon oxides (CO_2) as the oxidation gas after pyrolysis under an inert atmosphere. Annealing in CO_2 converts the Co species into Co_3O_4, while the excess carbon matrix is consumed. By controlling the carbonization time and temperature, Co_3O_4 particles with a certain carbon coating are obtained through calcination of the rod-like Co-MOF-74 crystals, whose structure is composed of infinite $Co_3O_3(CO_2)_3$ rods and 2,5-dioxidoterephthalate linkers, where each metal ion is coordinated to three carboxyl and two hydroxyl groups and a coordinated ligand [*N*,*N*-dimethylformamide (DMF) or water].[32] The particle size of Co_3O_4 is around 12 nm and this oxide is homogeneously dispersed in the carbon matrix. As expected, when evaluated as an anode for lithium ion batteries, this hybrid exhibits a higher specific capacity, better cyclability and excellent rate performance than the thick carbon-coated electrodes and pure Co_3O_4 electrodes.

Experimental

Synthesis of Co_3O_4@C composites

Synthesis of Co-MOF-74. The synthetic conditions of Co-MOF-74 were modified from those in the literature procedure.[33] 0.241 g H_4DOBDC (2,5-dihydroxyterephthalic acid) and 1.1885 g $Co(NO_3)_2 \cdot 6H_2O$ were dissolved in a mixture of DMF–ethanol–H_2O (v/v/v = 1 : 1 : 1, 100 mL) in a 125 mL Teflon-lined steel autoclave. The autoclave was tightly capped and heated in an oven at 100 °C for 24 h. The as-prepared red-orange crystals were filtered and washed with *N*,*N*-dimethylformamide (DMF) and methanol, sequentially, and finally dried at 150 °C under vacuum for 12 h to obtain the rod-shaped Co-MOF-74 crystals.

Synthesis of Co_3O_4@C composite. The as-prepared Co-MOF-74 was first carbonized at 700 °C for 2 h at a ramping rate of 5 °C min^{-1} under an argon flow to give a Co@C composite. Then, the Co@C composite was calcined at 500 °C for 1 h at a ramping rate of 5 °C min^{-1} under a CO_2 flow. A thick-carbon coated sample (denoted as Co@CoO@C) was obtained using the same procedure except that the calcination time was 30 min. Moreover, pure Co_3O_4 nanocrystals were obtained by directly carbonizing the Co@C composite at 250 °C for 2 h under an air atmosphere.

Materials characterization

The obtained products were characterized *via* XRD (BRUKER D8 ADVANCED, Cu Kα = 1.54 Å) at a scan rate of 0.02° s^{-1} from 10° to 80°. The operating voltage and current were kept at 40 kV and 40 mA, respectively. The BET surface area and pore volume of the materials were calculated from isothermal nitrogen sorption measurements at 77 K using a Quantachrome Autosorb-IQ gas adsorption analyzer. The general morphologies of the synthesized composites were examined *via* SEM using an SEM-HITACHI S-4800 and TEM using an FEI Tecnai T20. HRTEM images were recorded using an FEI Tecnai F20. Raman spectroscopic analysis was performed with a LabRAM HR800 with the laser excitation energy of 632.8 nm. Elemental analysis was performed on a Vario EL elemental analyzer. XPS measurements were performed on a Kratos Axis Ultra Imaging photoelectron spectrometer using a monochromatic Al Kα line (1486.7 eV). TGA was carried out on an SDT Q600 analyzer at a heating rate of 5 °C min^{-1} in a flowing air atmosphere.

Cell assembly and testing

The working electrode was composed of active material (80 wt%), Super P (10 wt%) and poly(vinylidene difluoride) (PVDF, 10 wt%). These materials were dissolved in *N*-methyl pyrrolidone (NMP) and sonicated until a homogenous slurry was formed. The slurry was then spread onto nickel foam, and pressed and dried under vacuum at 120 °C for 12 h. After the drying process, the foam was further pressed under a pressure of 20 MPa. Coin cells were finally assembled in an argon-filled glovebox with the as-prepared materials as the test electrode, metallic lithium as the counter and reference electrode, 1 M $LiPF_6$ in EC : DMC (1 : 1 in volume) as the electrolyte, and Whatman GF/D borosilicate glass-fiber sheets as the separator. The coin cells were cycled galvanostatically in the voltage range of 0.005–3.00 V at a current density of 100 mA g^{-1} with a multichannel battery test system (NEWARE). Cyclic voltammetry measurements were conducted with an RST electrochemical workstation at the scanning rate of 0.5 mV s^{-1} between 0.005 V and 3.00 V (*vs.* Li/Li^+). Electrochemical impedance spectroscopy (EIS) was conducted on a Zahner Zennium electrochemical workstation in the frequency range from 0.01 Hz to 100 000 Hz using a sine wave with an amplitude of 5.0 mV.

Results and discussion

The formation process for the Co_3O_4@C composite is illustrated in Scheme 1. Typically, Co-MOF-74 was first synthesized under hydrothermal conditions according to the reported method. The obtained Co-MOF-74 rods were first carbonized under an inert atmosphere for 2 h to be derived into the Co@C hybrids.

The Co@C samples were further calcined under a carbon dioxide flow for a certain time, where cobalt particles were oxidized into cobalt oxides, and at the same time the thick

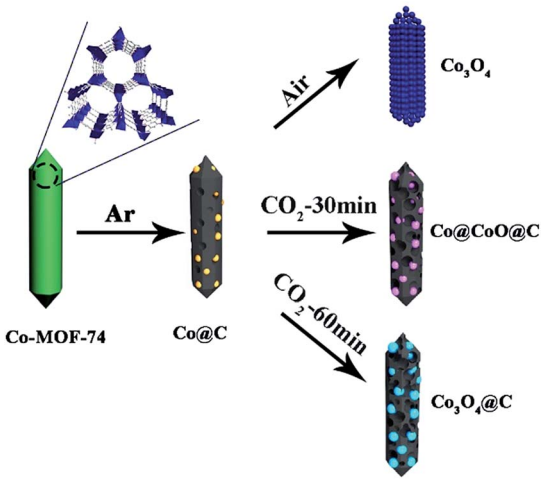

Scheme 1 Schematic of the synthetic process of the Co_3O_4@C composite.

carbon shells around the metal species were also consumed *via* oxidation. Finally, a thin carbon shell coated Co_3O_4 hybrid was formed (denoted as Co_3O_4@C). It is interesting to find that the final Co_3O_4@C composites still exhibited rod-like morphology, and the as-formed Co_3O_4 nanoparticles were homogeneously dispersed in the carbon matrix. The as-prepared materials showed mesoporous structures, which could facilitate the diffusion of Li^+ and electrolyte to enhance the kinetic properties of electrodes. For comparison, samples with a thick carbon shell (denoted as Co@CoO@C) and without the carbon coating (denoted as Co_3O_4) were prepared by shortening the CO_2 annealing time and direct oxidation in air, respectively. The powder X-ray diffraction (XRD) patterns of the as-synthesized Co-MOF-74 crystals were well-consistent with the simulated patterns, as shown in Fig. S1 in the ESI† which confirms the high quality of the obtained samples. The SEM images (Fig. S2, ESI†) show that all the Co-MOF-74 crystals possess a rod-like morphology with smooth surfaces, clear facets and high length–diameter ratio, which suggest the high crystallinity of the MOFs. A typical type-I isothermal curve is observed from the nitrogen adsorption/desorption measurement of the Co-MOF-74 rods, with a calculated Brunauer–Emmett–Teller (BET) surface area of 1025 $m^2\ g^{-1}$ and pore volume of 0.48 $cm^3\ g^{-1}$, which confirm the microporosity of the MOFs (Fig. S3a, ESI†). Fig. S3b† shows a narrow pore size distribution (fitted using the Nonlinear Density Functional Theory (NLDFT) model) with only one peak at ~0.5 nm, which corresponds to the one dimensional (1D) channels in the hexagonal MOF-74 matrix. The thermal treatment procedure was established according to the thermogravimetric analysis (TGA) results. From the TGA curve of pure Co-MOF-74 under an inert atmosphere, the first weight loss before 100 °C came from the evaporation of remnant solvents, such as DMF and ethanol, whereas the second weight loss at around 500 °C was due to the destruction of the MOF structures (Fig. S4, ESI†). The MOFs worked as a sacrificial self-template and underwent complicated reactions during the pyrolysis process, where the carbonization of organic components and reduction of metal species happened simultaneously. To ensure the complete reduction of Co and remove unstable carbon species, a high temperature of 700 °C was chosen for the first thermal treatment step. The diffraction peaks of the products match well with the pure Co phase with a cubic structure, which confirms the formation of metallic Co (Fig. S5, ESI†) and the rod shape of the mother crystals was also well-reserved during this process (Fig. S6, ESI†). The obtained Co@C samples were further treated in different atmospheres of air and CO_2, separately (Fig. S7, ESI†). It is clear that under air atmosphere, the Co nanoparticles were easily oxidized at a low temperature of 150 °C, accompanied by the complete removal of the carbon matrix. This process was completed at 250 °C, leaving only a trace amount of carbon in the final products (Table S1, ESI†). On the other hand, under the much milder oxidation atmosphere of flowing CO_2, the gradual oxidation of Co nanoparticles and carbon evaporation happened simultaneously at a much slower rate until 600 °C, where an abrupt weight loss took place due to the vigorous reaction between the carbon matrix and CO_2. Accordingly, the temperatures of 250 °C and 500 °C were chosen for annealing in air and CO_2 atmosphere, respectively, in the second thermal treatment step.

The crystal and phase information of the as-synthesized Co@C, Co_3O_4, Co@CoO@C and Co_3O_4@C composites were confirmed by XRD, as shown in Fig. 1. After the first heat treatment step, the Co@C composite was obtained, where nanosized cobalt nanoparticles formed *in situ* and dispersed uniformly in the porous carbon matrix. After the oxidation process, the XRD pattern of the Co_3O_4 composites is consistent with the theoretical patterns of Co_3O_4 with a face-centered cubic lattice (JCPDF No. 42-1467), whereas the Co_3O_4 and Co_3O_4@C composites show similar diffraction peaks, which indicates that the main phase of both nanocomposites is identical. It is noteworthy that no diffraction peaks of CoO or Co were present for these two samples, which proves the complete oxidation of the Co species. On the other hand, for the Co@CoO@C nanocomposites, it is evident that there are strong peaks belonging to metallic Co, whereas the other weak peaks are attributed to CoO species. The diffraction of Co_3O_4 was not observed, which

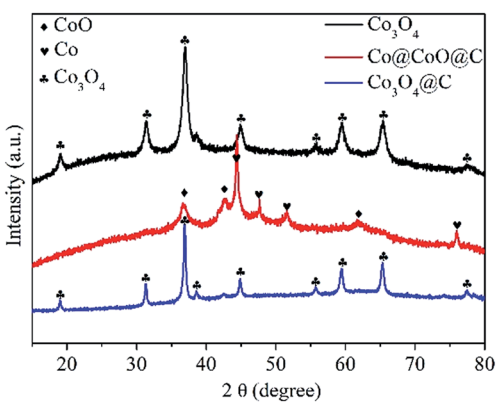

Fig. 1 XRD patterns of the Co_3O_4, Co@CoO@C and Co_3O_4@C composites derived from the pyrolysis of Co-MOF-74 under various gas atmospheres and temperatures.

implies that the Co nanoparticles were only partially oxidized. These results indicate that the oxidation of Co species in CO_2 proceeds stepwise: first in the metastable CoO phase, and then after the complete consumption of metallic Co, the oxidation of CoO in the thermodynamically-stable Co_3O_4 phase could take place. It is proven that control over the annealing time in CO_2 is crucial for the phase composition of the final products. A shortened annealing time could lead to the incomplete consumption of metallic Co and halfway oxidation into a metastable CoO phase due to more sluggish reaction kinetics in CO_2 compared to that in air, which is consistent with TGA results.

The typical scanning electron microscopy (SEM), transmission electron microscopy (TEM) and high resolution transmission electron microscopy (HRTEM) images of the Co_3O_4, Co@CoO@C and Co_3O_4@C composites are shown in Fig. 2. The inserted pictures show an individual particle of each composite. In Fig. 2a–c, it is shown that the original rod shape of the mother MOFs is well-reserved for all three composites, although some cracks could be seen in the Co_3O_4 sample, which are caused by the severe structural change during the direct heat treatment in air. No such cracks were found in the Co@CoO@C and Co_3O_4@C composites, and some irregular edges indicate the residue of amorphous carbon, which is also evidenced by the TEM images. Fig. 2d–f show the TEM images of the Co_3O_4, Co@CoO@C and Co_3O_4@C composites, respectively. From Fig. 2d it can be seen that the rods of Co_3O_4 are actually composed of aggregated Co_3O_4 nanoparticles with an average size of *ca.* 12 nm. In the HRTEM image in Fig. 2g, lattice fringes are observed with the measured lattice spacing of 0.233 nm, which correspond to the (222) crystal planes of Co_3O_4, and it is clear that the Co_3O_4 particles agglomerated without any coating on their surface. On the contrary, for the CO_2-treated samples, spherical cobalt oxide nanoparticles are dispersed in the carbon matrix, as shown in Fig. 2e and f. The carbon layer coating on the surface of the cobalt oxide particles could be easily distinguished for both Co@CoO@C and Co_3O_4@C from the HRTEM images in Fig. 2h and i, respectively. For the Co@CoO@C sample, the thickness of the carbon shells is ~14 nm, whereas for Co_3O_4@C much thinner shells ranging from 2–6 nm are observed. These results imply that by controlling the calcination time in the CO_2 flow at moderate temperature, a certain amount of carbon could be controlled using our method. Just by changing the carbonization time, the content and thickness of the coated carbon could be controlled to an optimal level to facilitate the diffusion of Li^+ through the shell and conductivity of the hybrids for enhanced electrochemical performances. The Raman spectra of the as-synthesized composites were investigated to illustrate the graphitization degree of carbon (Fig. S8, ESI†). As shown by the Raman spectra, the Co@C, Co_3O_4@C and Co@Co@C samples display two distinguishable peaks in the range of 1000–2000 cm^{-1}. The peak located at around 1350 cm^{-1} is attributed to the D band, whereas the peak at around 1590 cm^{-1} is from the G band. An increased intensity ratio in the I_D/I_G ratios indicates the transitional stage from amorphous carbon to crystalline graphite.[34] The I_D/I_G ratio is close to 0.86 for Co@C and about 0.91 for Co@CoO@C, whereas for Co_3O_4@C the ratio is 1.34 (Fig. S8, ESI†). This indicates that the Co_3O_4@C samples possess the highest graphitization degree, and more defects and edges exposed for carbon, which could enhance the electron conductivity of these hybrids and give more sites to store Li^+. Element analysis was conducted to determine the carbon content in the hybrids, and the results are shown in Table S1 (ESI†). The carbon content for the Co@C samples is 12.38 wt%, whereas after CO_2 treatment for 30 min, the content decreases to 10.7 wt%. When the treatment time increased to 60 min, the percentage was lowered to only 3.17 wt%. For pure Co_3O_4 samples, only a trace amount of carbon was detected. These results are consistent with the HRTEM image analysis that the content and thickness of carbon shell are controlled by changing the calcination atmosphere and time.

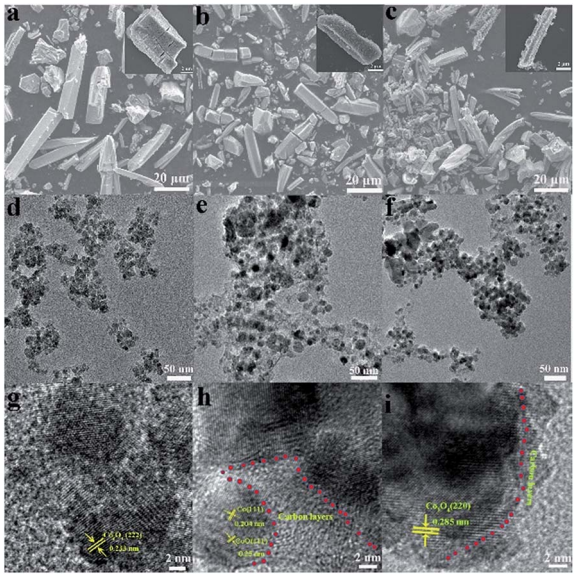

Fig. 2 SEM images of the (a) Co_3O_4, (b) Co@CoO@C and (c) Co_3O_4@C composites. TEM images of the (d) Co_3O_4, (e) Co@CoO@C and (f) Co_3O_4@C composites. HRTEM images of the (g) Co_3O_4, (h) Co@CoO@C and (i) Co_3O_4@C composites.

X-ray photoelectron spectroscopy (XPS) was employed to further identify the surface composition and the oxidation state of Co in the composites (Fig. 3). The full XPS spectra show the existence of Co, C and O, which is in accordance with the element analysis, as shown in Fig. 3a. The peak intensity of carbon for Co_3O_4@C is much weaker than that of the Co@CoO@C sample, which indicates a lower carbon content in the former hybrid, whereas the pure Co_3O_4 sample shows almost no carbon signal, which confirms its ultra-low carbon content. In the high-resolution XPS spectrum of Co 2p for the Co_3O_4 composites in Fig. 3b, there are two peaks located at 795.4 eV (Co $2p_{1/2}$) and a low energy band at 780.4 eV (Co $2p_{3/2}$). The energy difference between the Co $2p_{1/2}$ and Co $2p_{3/2}$ splitting is 15 mV, which indicates the existence of Co^{2+} and Co^{3+} and corresponds to the existence of Co_3O_4. Two satellite peaks near the Co 2p peaks are also observed.[35] The Co 2p spectrum of the Co_3O_4@C composite is similar to that of Co_3O_4, which is consistent with the XRD patterns that both samples contain

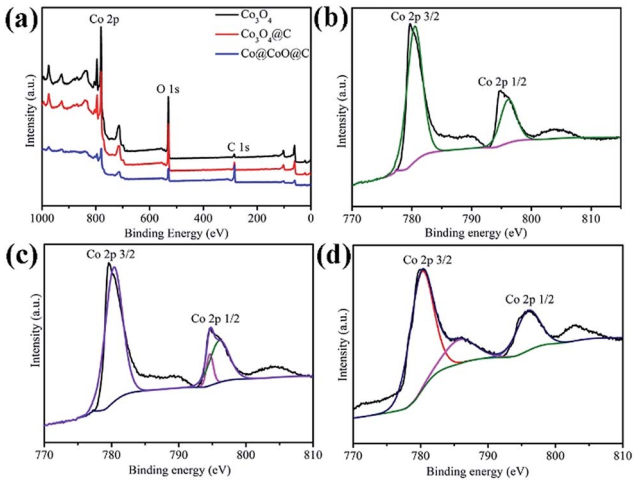

Fig. 3 View of (a) full XPS spectra of the Co_3O_4, Co_3O_4@C and Co@CoO@C composites. High-resolution XPS spectra of Co 2p for the (b) Co_3O_4, (c) Co_3O_4@C and (d) Co@CoO@C composites.

Co_3O_4, as shown in Fig. 3c. However, in the Co 2p spectrum of the Co@CoO@C composite in Fig. 3d, there are two peaks corresponding to the high energy band (796.1 eV) and low energy band (780.2 eV), which are attributed to the Co $2p_{1/2}$ and Co $2p_{3/2}$ binding energies of CoO. These results confirm the existence of CoO in the composites.[36]

N_2-sorption measurements were conducted to investigate the specific surface areas and porous features of all the composites, as shown in Fig. 4 and S9 (ESI†). All the composites exhibit type IV isotherms (IUPAC definition) with evident hysteresis loops, which indicate their mesoporous nature. The specific surface areas were calculated based on the multi-point BET method, and the NLDFT method was used to analyze the pore size distribution for all the samples. The Co@C composite shows a high BET surface area of 133 $m^2\ g^{-1}$ (Fig. S9a, ESI†) and pore volume of 0.23 $cm^3\ g^{-1}$, with a single pore size distribution peak from 3.0 nm to 15.0 nm (Fig. S9b, ESI†). After CO_2 calcination, the surface areas decrease from 121 $m^2\ g^{-1}$ for Co@CoO@C to 76 $m^2\ g^{-1}$ for Co_3O_4@C as the heat treatment time is extended from 30 min to 60 min, which is due to the consumption of the amorphous porous carbon matrix. The Co_3O_4 sample, on the other hand, presents a high surface area of 101 $m^2\ g^{-1}$. The pore size distribution of these three samples shows generally two types of pores: a micropore of *ca.* 2.0 nm and another larger pore from 2.5 nm to the mesoporous range. The pore size ranges from 1.1 to 4.2 nm for the Co@CoO@C composite, whereas for the Co_3O_4@C composite the pore size is between 1.5 and 2.7 nm. The Co_3O_4@C composite shows less mesopores than Co@CoO@C due to the collapse of the unstable hole walls during the heat treatment. The Co_3O_4 sample, however, shows a larger mesopore component ranging from 2.5 to 11.0 nm, which originates from the vigorous gas evolution in direct air calcination. The mesoporous structure of these composites may be beneficial for improving electrochemical performances by facilitating the diffusion of electrolyte into the matrix and exposing more active sites reacting with Li^+.

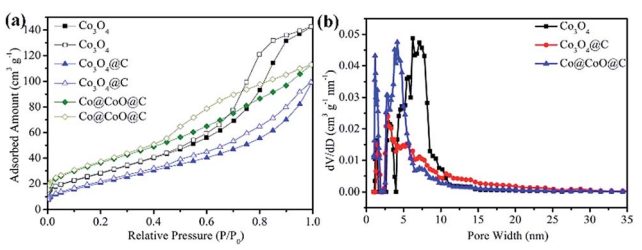

Fig. 4 (a) N_2 adsorption/desorption isotherm curves and (b) pore size distributions of the Co_3O_4, Co_3O_4@C and Co@CoO@C composites.

The electrochemical performance of the Co_3O_4, Co@CoO@C and Co_3O_4@C composites were investigated, as shown in Fig. 5. The first and second charge–discharge curves of the Co_3O_4@C composite were tested at a current density of 100 mA g^{-1} between 0.005 and 3.0 V (Fig. 5a). During the first cycle, the plateau at 1.0 V is ascribed to the lithiation of Co_3O_4 forming $Li_xCo_3O_4$.[37] Although the voltage was further decreased, the plateau below 1.0 V is followed by a long slope corresponding to the conversion reaction and the formation of an SEI film on the surface of the electrode, particularly for metal oxides materials.[38] The initial charge and discharge capacities were 1165 mA h g^{-1} and 1857 mA h g^{-1}, respectively, showing an irreversible capacity loss of 37%. Fig. 5b shows that the first charge and discharge capacities were 448 and 822 mA h g^{-1} for the Co@CoO@C composite, respectively, and the irreversible capacity loss was about 45%. The first charge and discharge capacities were 594 and 961 mA h g^{-1}, respectively, with the irreversible capacity loss of 38% for Co_3O_4 electrode in Fig. 5c. All these electrodes show large irreversible capacities, which may be attributed to the formation of a solid electrolyte interphase (SEI) film during the discharge process and to the irreversible decomposition of the electrolyte.[39] However, the Co@CoO@C electrodes show a larger capacity loss than the Co_3O_4 and Co_3O_4@C electrodes. The high content of amorphous carbon in this composite that could react with lithium consumed more lithium-ions, which led to the large

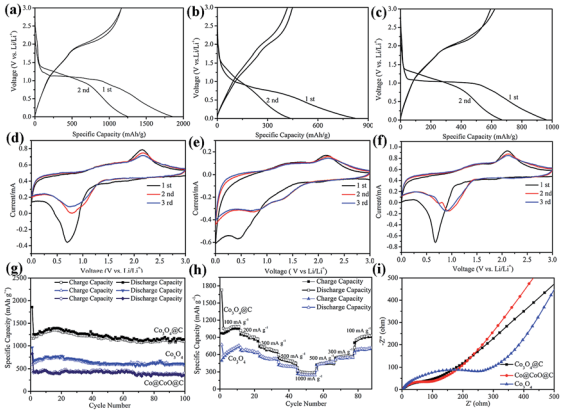

Fig. 5 Electrochemical properties of the (a) first and second charge–discharge curves of Co_3O_4@C, (b) Co@CoO@C and (c) Co_3O_4 electrodes. Cyclic voltammogram (CV) profiles of the (d) Co_3O_4@C, (e) Co@CoO@C and (f) Co_3O_4 electrodes. Cycling performances at (g) a current density of 100 mA g^{-1} and (h) varied current densities from 0.1 to 1.0 A g^{-1}. (i) Electrochemical impedance spectra of the three electrodes.

capacity loss during the first cycle.[40] After the first cycle, the coulombic efficiencies above 98% of the electrodes indicate good reversibility of these electrodes. To further investigate the electrochemical process, CV profiles of the electrodes are shown in Fig. 5d–f between 0.005 and 3.0 V at a scan rate of 0.5 mV s^{-1}. In the first cycle, the peak located at 0.6 V for the Co_3O_4@C electrode is attributed to the formation of an SEI film on the electrode surface in Fig. 5d. During the second cycle, there is a peak located at 0.75 V, which is attributed to the lithiation of Co_3O_4, and an oxidation peak located at 2.1 V corresponding to the delithiation process and the recovery of Co_3O_4.[41] Both the reduction and oxidation peaks shift in the subsequent cycle, which is common for metal oxide electrodes. These results are consistent with the charge–discharge plateaus. There are several CV profiles for the Co@CoO@C electrode, as shown in Fig. 5e, and it is evident that during the first cycle, there is a peak located at 0.5 V corresponding to the formation of an SEI film after the first cycle. The reduction peak-shift to 0.7 V is attributed to the lithiation of CoO to form Li_xCoO.[42] After the first cycle, there are two cathodic peaks located at 0.7 V and 1.3 V, which correspond to the electrochemical reaction between CoO and Li^+.[43] For the pure Co_3O_4 electrode, the 0.7 V peak is also attributed to the formation of an SEI film on the electrode surface. After the first cycle, the weak cathodic peak shifts to 1.0 V during the following cycles, which is also consistent with the Co_3O_4 electrode. However, the anodic peaks for the Co_3O_4 electrode located at 2.2 V are from the oxidation of Co to Co_3O_4 in Fig. 5f. The long-term stability cycling performance of the Co_3O_4, Co_3O_4@C and Co@CoO@C electrodes is presented in Fig. 5g. The second charge and discharge capacities are 1167 mA h g^{-1} and 1255 mA h g^{-1} for the Co_3O_4@C electrode, and even after 100 cycles the charge capacity remains at 1095 mA h g^{-1} and the discharge capacity is 1137 mA h g^{-1}, which correspond to a high capacity retention of 96% compared with the second cycle charge capacity. This superior performance is comparable with previous reports (Table S2, ESI†). However, the pure Co_3O_4 and Co@CoO@C electrodes only exhibit a discharge capacity of 593 and 355 mA h g^{-1}, respectively, after the 100 cycles test. From the HRTEM test, it is clear that the carbon shell thickness of the Co_3O_4@C composite is 2–6 nm, whereas the thickness of the Co@CoO@C composite is about 14 nm, in which a thin carbon shell could facilitate the diffusion of mass and electrons. These results confirm that the thin carbon shell coating benefits the electrochemical performance by enhancing electron conductivity and making full use of the active materials. However, for the Co@CoO@C electrode, pure Co particles dominate the main part of the entire hybrid, which do not contribute to the electrochemical performance of the electrode. The rate performances of the electrodes are shown in Fig. 5h. The current range is from 100 mA g^{-1} to 1 A g^{-1}. The reversible capacity reached 1090, 1020, 867, 682, and 447 mA h g^{-1} when tested at 100, 200, 300, 500, and 1000 mA g^{-1}, respectively. When the current density decreased to 100 mA g^{-1}, the revisable capacity returned to 1084 mA h g^{-1}, which indicates the stable structure of the electrodes.[44] Notably, the capacities of the pure Co_3O_4 electrode were far less than those of the Co_3O_4@C electrode. The reversible capacity reached 730, 640, 510, 383, and 240 mA h g^{-1} when tested at the same current density as that of Co_3O_4@C. After the current decreases to 100 mA g^{-1}, the revisable capacity goes back to 704 mA h g^{-1}. These results confirm that the rate performance of the Co_3O_4@C electrode is better than that of the Co_3O_4 electrode, which implies good structure stability of the Co_3O_4@C electrode. It is inferred that the thin carbon shell coating on the electrode inhibits capacity decay by buffering the volume changes during the lithium insertion and extraction processes.[45] Electrochemical impedance spectroscopy (EIS) was employed to investigate the good electrochemical performance of these three electrodes, as shown in Fig. 5i. All three plots in this figure are composed of a semicircle in the high to medium frequency region, followed by a sloped line in the low frequency region. The semicircle is associated with the charge transfer resistance at high frequency. The impedance is associated with the charge transfer resistance between the electrode and electrolyte and the slope line at the low frequency is associated with the resistance in the electrode.[46,47] The resistance of Co_3O_4@C was significantly lower than that of the Co_3O_4 electrode, whereas the resistance of the Co@CoO@C electrode was almost the same as that of the Co_3O_4@C electrode. We used the equivalent circuit to fit the data. R_s and R_{ct} are the ionic resistance of the electrode and the charge transfer resistance, respectively.[48a] Z_W is the Warburg impedance, and CPE is the constant phase-angle element involving the double layer capacitance.[48] From the calculated data, R_{ct} for Co_3O_4, Co@CoO@C, and Co_3O_4@C is 14.73 Ω, 4.26 Ω, 3.70 Ω, respectively. It is clear that the R_{ct} of the Co_3O_4@C composite is smaller than that of the Co_3O_4 and Co@CoO@C composites, which indicates good electrolyte infiltration and charge-transport capability (Fig. S10, ESI†). The electronic conductivity was enhanced and it thus enabled easier charge transfer between the electrode and electrolyte interface in the Co_3O_4@C electrode. Thus, carbon coating is important to enhance the electron conductivity to improve the electrochemical performance.

Conclusions

In summary, thin carbon shell coated Co_3O_4 particles were prepared *via* the CO_2 oxidization of porous MOF materials. The as-synthesized Co_3O_4@C electrode exhibits a higher specific capacity and excellent rate performance compared to the bare Co_3O_4 electrode, which is attributed to the small particle size and thin carbon shell buffering the volume change the during lithiation and delithiation processes as well as enhancing the electron conductivity. This study provides a new method to fabricate composites derived from porous MOF nanostructures and it may provide a new approach for the synthesis of metal oxide composites with enhanced properties for energy storage in lithium-ion batteries.

Acknowledgements

This study was financially supported by the National Natural Science Foundation of China (No. 51322205 and 21371014) and the National Program for Support of Top-notch Young Professionals, and the Beijing Municipal Science & Technology Commission Program (Z151100000915074).

References

1 P. G. Bruce, S. A. Freunberger, L. J. Hardwick and J. M. Tarascon, *Nat. Mater.*, 2012, **11**, 19–29.
2 W. Xia, A. Mahmood, R. Q. Zou and Q. Xu, *Energy Environ. Sci.*, 2015, **8**, 1837–1866.
3 M. Barghamadi, A. S. Best, A. I. Bhatt, A. F. Hollenkamp, M. Musameh, R. J. Reesc and T. Ruthera, *Energy Environ. Sci.*, 2014, **7**, 3902–3920.
4 P. Poizot, S. Laruelle, S. Grugeon and J. M. Tarascon, *J. Electrochem. Soc.*, 2002, **149**, A1212–A1217.
5 J. Jiang, Y. Y. Li, J. P. Liu, X. T. Huang, C. Z. Yuan and X. W. Lou, *Adv. Mater.*, 2012, **24**, 5166–5180.
6 M. V. Reddy, G. V. Subba Rao and B. V. R. Chowdari, *Chem. Rev.*, 2013, **113**, 5364–5457.
7 J. F. Zhang, W. Y. Ren, Y. Y. Zhou, P. Li, L. Xu, D. M. Sun, P. Wu, Y. M. Zhou and Y. W. Tang, *Chem.–Eur. J.*, 2016, **22**, 9599–9606.
8 K. M. Nam, J. H. Shim, D. W. Han, H. S. Kwon, Y. M. Kang, Y. Li, H. Song, W. S. Seo and J. T. Park, *Chem. Mater.*, 2010, **22**, 4446–4454.
9 A. K. Rai, J. Gim, L. T. Anh and J. Kim, *Electrochim. Acta*, 2013, **100**, 63–71.
10 J. Y. Wang, N. L. Yang, H. J. Tang, Z. H. Dong, Q. Jin, M. Yang, D. Kisailus, H. J. Zhao, Z. Y. Tang and D. Wang, *Angew. Chem., Int. Ed.*, 2013, **52**, 6417–6420.
11 H. H. Li, Z. Y. Li, X. L. Wu, L. L. Zhang, C. Y. Fan, H. F. Wang, X. Y. Li, K. Wang, H. Z. Sun and J. P. Zhang, *J. Mater. Chem. A*, 2016, **4**, 8242–8248.
12 J. Y. Wang, N. L. Yang, H. J. Tang, Z. H. Dong, Q. Jin, M. Yang, D. Kisailus, H. J. Zhao, Z. Y. Tang and D. Wang, *Angew. Chem., Int. Ed.*, 2013, **125**, 6545–6548.
13 H. Guo, T. T. Li, W. W. Chen, L. X. Liu, X. J. Yang, Y. P. Wang and Y. C. Guo, *Nanoscale*, 2014, **6**, 15168–15174.
14 F. Zhang, C. Z. Yuan, J. J. Zhu, J. Wang, X. G. Zhang and X. W. Lou, *Adv. Funct. Mater.*, 2013, **23**, 3909–3915.
15 F. B. Hao, Z. W. Zhang and L. W. Yin, *ACS Appl. Mater. Interfaces*, 2013, **5**, 8337–8344.
16 H. Li, M. Eddaoudi, M. O'Keeffe and O. M. Yaghi, *Nature*, 1999, **402**, 276–279.
17 S. L. Li and Q. Xu, *Energy Environ. Sci.*, 2013, **6**, 1656–1683.
18 Q. L. Zhu and Q. Xu, *Chem. Soc. Rev.*, 2014, **43**, 5468–5512.
19 Y. Zhao, Z. Song, X. Li, Q. Sun, N. Cheng, S. Lawes and X. Sun, *Energy Storage Materials*, 2016, **2**, 35–62.
20 X. D. Xu, R. G. Cao, S. Jeong and J. Cho, *Nano Lett.*, 2012, **12**, 4988–4991.
21 F. C. Zheng, G. L. Xia, Y. Yang and Q. W. Chen, *Nanoscale*, 2015, **7**, 9637–9645.
22 F. Zou, Y. M. Chen, K. W. Liu, Z. T. Yu, W. F. Liang, S. M. Bhaway, M. Gao and Y. Zhu, *ACS Nano*, 2016, **10**, 377–386.
23 W. X. Guo, W. W. Sun and Y. Wang, *ACS Nano*, 2015, **9**, 11462–11471.
24 H. Li, M. Liang, W. W. Sun and Y. Wang, *Adv. Funct. Mater.*, 2016, **26**, 1098–1103.
25 G. Huang, F. F. Zhang, X. C. Du, Y. L. Qin, D. M. Yin and L. M. Wang, *ACS Nano*, 2015, **9**, 1592–1599.
26 W. Xia, R. Q. Zou, L. An, D. G. Xia and S. J. Guo, *Energy Environ. Sci.*, 2015, **8**, 568–576.
27 A. Aijaz, J. Masa, C. Rosler, W. Xia, P. Weide, A. J. R. Botz, R. A. Fischer, W. Schuhmann and M. Muhler, *Angew. Chem., Int. Ed.*, 2016, **55**, 4087–4091.
28 R. B. Wu, X. K. Qian, K. Zhou, J. Wei, J. Lou and P. M. Ajayan, *ACS Nano*, 2014, **8**, 6297–6303.
29 F. Zou, X. L. Hu, Z. Li, L. Qie, C. C. Hu, R. Zeng, Y. Jiang and Y. H. Huang, *Adv. Mater.*, 2014, **26**, 6622–6628.
30 S. J. Yang, S. Nam, T. Kim, J. H. Im, H. Jung, J. H. Kang, S. G. Wi, B. Park and C. R. Park, *J. Am. Chem. Soc.*, 2013, **135**, 7394–7397.
31 (*a*) Q. F. Wang, R. Q. Zou, W. Xia, J. Ma, B. Qiu, A. Mahmood, R. Zhao, Y. Y. C. Yang, D. G. Xia and Q. Xu, *Small*, 2015, **11**, 2511–2517; (*b*) S. H. Ren, R. Prakash, D. Wang, V. S. K. Chakravadhanula and M. Fichitner, *ChemSusChem*, 2012, **5**, 1397–1400; (*c*) N. Yan, X. Zhou, Y. Li, F. Wang, H. Zhong, H. Wang and Q. W. Chen, *Sci. Rep.*, 2013, **3**, 3392.
32 L. J. Wang, H. X. Deng, H. Furukawa, F. Gándara, K. E. Cordova, D. Peri and O. M. Yaghi, *Inorg. Chem.*, 2014, **53**, 5881–5883.
33 S. R. Caskey, A. G. Wong-Foy and A. J. Matzger, *J. Am. Chem. Soc.*, 2008, **130**, 10870–10871.
34 A. C. Ferrari and J. Robertson, *Phys. Rev. B: Condens. Matter Mater. Phys.*, 2000, **61**, 14095–14107.
35 Y. Y. Liang, Y. G. Li, H. L. Wang, J. G. Zhou, J. Wang, T. Regier and H. J. Dai, *Nat. Mater.*, 2011, **10**, 780–786.
36 R. Gao, Z. Y. Li, X. L. Zhang, J. C. Zhang, Z. B. Hu and X. F. Liu, *ACS Catal.*, 2016, **6**, 400–406.
37 X. Yao, G. L. Guo, Y. Zhao, Y. Zhang, S. Y. Tan, Y. F. Zeng, R. Q. Zou, Q. Y. Yan and Y. L. Zhao, *Small*, 2016, **12**, 3849–3860.
38 S. L. Xiong, J. S. Chen, X. W. Lou and H. C. Zeng, *Adv. Funct. Mater.*, 2012, **22**, 861–871.
39 Y. H. Dou, J. T. Xu, B. Y. Ruan, Q. N. Liu, Y. D. Pan, Z. Q. Sun and S. X. Dou, *Adv. Energy Mater.*, 2016, **6**, 1501835.
40 J. L. Tang, V. Etacheri and V. G. Pol, *ACS Sustainable Chem. Eng.*, 2016, **4**, 2624–2631.
41 I. Sultana, M. M. Rahman, T. Ramireddy, N. Sharma, D. Poddar, A. Khalid, H. Z. Zhang, Y. Chen and A. M. Glushenkov, *ACS Appl. Mater. Interfaces*, 2015, **7**, 20736–20744.
42 S. H. Wang, M. Q. Chen, Y. Y. Xie, Y. N. Fan, D. W. Wang, J. J. Jiang, Y. G. Li, H. Grutzmacher and C. Y. Su, *Small*, 2016, **12**, 2365–2375.
43 Y. F. Dong, S. H. Liu, Z. Y. Wang, Y. Liu, Z. B. Zhao and J. S. Qiu, *RSC Adv.*, 2015, **5**, 8929–8932.
44 G. Y Huang, S. M. Xu, S. S. Lu, L. Y. Li and H. Y. Sun, *ACS Appl. Mater. Interfaces*, 2014, **6**, 7236–7243.
45 Y. Zhao, X. F. Li, B. Yan, D. B. Xiong, D. J. Li, S. Lawes and X. L. Sun, *Adv. Energy Mater.*, 2016, 1502175.
46 Y. M. Liu, X. Y. Zhao, F. Li and D. G. Xia, *Electrochim. Acta*, 2011, **56**, 6448–6452.
47 G. Chen, Z. Y. Wang and D. G. Xia, *Chem. Mater.*, 2008, **20**, 6951–6956.
48 (*a*) D. Wang, Q. Wang and T. Wang, *Inorg. Chem.*, 2011, **50**, 6482–6492; (*b*) Y. Tan, Q. Gao, Z. Li, Q. Tian, W. Qian, C. Yang and H. Zhang, *Sci. Rep.*, 2016, **6**, 26460.